OXFORD

Oxford Open Materials Science, 2023, **3(1)**, itac015

https://doi.org/10.1093/oxfmat/itac015
Advance Access Publication Date: 9 January 2023
Research article

Large enhancement of thermal conductivity of aluminum-reduced graphene oxide composites prepared by a single-step method

Arijit Mitra [1,2,§], Mihir Ranjan Sahoo[2,§], Aiswarya Samal[2], Sunil Kumar Pradhan[2,3], Balaram Polai[2], Krishna Rani Sahoo[4], Subrat Kar[5], Bijoy Kumar Satpathy[2], Tharangattu N. Narayanan [4], Pulickel M. Ajayan[6], Parlapalli V. Satyam[1,2], Saroj K. Nayak[2,*]

[1]Institute of Physics, Bhubaneswar, Odisha, 751005, India
[2]School of Basic Sciences, Indian Institute of Technology, Bhubaneswar, Odisha, 752050, India
[3]School of Electronics Engineering, Vellore Institute of Technology, Chennai, Tamil Nadu, 600127, India
[4]Tata Institute of Fundamental Research-Hyderabad, Hyderabad, Telangana, 500046, India
[5]National Aluminium Company, Bhubaneswar, Odisha, 751013, India
[6]Department of Materials Science and Nano Engineering, Rice University, Houston, Texas, 77005, USA

*Correspondence address. School of Basic Sciences, Indian Institute of Technology Bhubaneswar. Argul, Khordha, Odisha, 752050, India. E-mail:nayaks@iitbbs.ac.in (S.K.N)
[§]Both authors have equal contribution.

Abstract

Metal matrix composites have attracted extensive attention from both the research and industrial perspective. In this study, we prepared aluminum-reduced graphene oxide (Al–rGO) composites with enhanced thermal conductivity in an easy single-step process. Pristine Al shows a thermal conductivity of 175 $Wm^{-1}K^{-1}$ (standard deviation <5%), which increases to 293 $Wm^{-1}K^{-1}$ for an Al–rGO composite with 1% rGO. Analysis of theoretical models shows that a higher percentage of rGO inside the Al matrix creates a continuous network resulting in more available phase space through which heat carrier phonons travel with less scattering, and hence thermal conductivity of the composite increases. Furthermore, Al–rGO composites show an ∼5% increase in microhardness compared with pristine Al. The electrical resistivity of the composite is comparable to that of pristine Al for a narrow weight percentage of rGO, whereas a 70% enhancement in the thermal conductivity of the composite is observed for the same weight percentage range, suggesting possibilities for exploiting both high electrical and thermal conductivities for various applications.

Keywords: aluminum, metal matrix composite, thermal conductivity, reduced graphene oxide, Maxwell model, density functional theory

Introduction

Metal matrix composites are an exciting research topic and have numerous industrial applications, especially in aerospace, automobile industries, thermal management, etc. These two-phase composite materials are prepared by combining one material with a continuous phase (matrix) and another with a discontinuous phase (filler particles) dispersed in the matrix displaying several unique properties which cannot be achieved by a single-phase material alone [1–8]. Therefore, researchers have devoted tremendous effort to designing suitable composite materials according to the desired application. The structural and functional properties of the composite materials can be modified as per the requirement of the specific applications by selecting suitable materials and reinforcement processes [8]. Multifunctional graphene-based composites, such as polymer/graphene or metal/graphene have been very popular among researchers owing to graphene's superior electrical and thermal conductivities, excellent mechanical strength and high carrier mobility [9, 10].

Aluminum (Al) is one of the most advantageous metals for a range of applications because of its high electrical conductivity, thermal conductivity, low density and cost-effectiveness [3, 4, 6, 11]. However, for a few applications (such as conductors or interconnects, and cooking utensils), an improved electrical and/or thermal conductivity of Al would enable it to replace existing expensive metals, such as Cu. A significant enhancement of the thermal and electrical properties of Al can be achieved by incorporating a low-weight percentage of graphene into the Al matrix. The reports on Al–graphene composites in the literature primarily focus on mechanical properties [7, 12–17]. For example, Wang *et al.* reported 62% higher tensile strength in aluminum–reduced graphene oxide (Al–rGO) composites compared with pure Al [12]. Similarly, there are additional reports in the literature where the mechanical strength of Al–rGO composites has been studied and the importance of these composites has been shown in the automobile industry [13–15]. A few researchers have studied the electrical conductivity of Al–carbon nanotubes [18, 19]; however, studies on the electrical and thermal properties of Al–rGO composites are comparatively unexplored. Al has a thermal conductivity (K) of 247 $Wm^{-1}K^{-1}$, whereas the K value for rGO can reach up to 2600 $Wm^{-1}K^{-1}$ [20]. Therefore, the incorporation of a small

Received: November 10, 2022. **Revised:** December 06, 2022. **Accepted:** December 12, 2022

amount of rGO into the Al matrix may effectively reinforce the thermal conductivity (K) of the composite. In this study, we aim to focus on the electrical and thermal conductivities of Al–rGO composites in order to realize their potential application as conductors.

Moreover, the commonly used preparation technique for Al–rGO composites is the powder metallurgy method [7, 13, 15, 21–23]. In the first stage of this two-step process, Al and rGO powder are ball-milled. Then a pellet is prepared from the powder mixture and sintered approximately at 670°C. A few researchers used a solution-assisted mixing process, where the Al and rGO powders are dispersed in a suitable solvent and sonicated [23–25]. As compared to the ball-milling method, solution-assisted mixing is advantageous as it poses a lower risk of creating defects in rGO and contamination in the composites. However, solution-assisted mixing requires a solvent, which may react with the powders and oxidizes Al [23]. Further, the moist media often affect the consolidation process. Although these methods are well-established and efficient for preparing the Al–rGO composites, these methods are not suitable to produce electrical conductors or interconnect at an industrial scale. The primary reasons include difficulties in casing at the industrial scale and oxidation of Al powder. Although there are studies on the incorporation of carbon in the molten Al [26], however, a similar approach using graphene has not been reported. Therefore, a facile, scalable and industry-friendly approach for preparing the Al–rGO composite has been another primary motivation for the present work.

Herein, we propose a simple method to prepare Al–rGO composites by heating Al metal and rGO powder together at 700°C. This method is one-step and can be easily scaled up for industrial production by casting technique. Moreover, as this process uses an Al metal sheet instead of Al powder, higher electrical conductivity and lower oxidation can be achieved. Raman mapping and energy dispersive X-ray spectroscopy (EDS) mapping of the as-prepared samples showed an isotropic distribution of rGO in the Al matrix. Thermal conductivities (*K*) of Al–rGO composites were experimentally measured, and compared with pristine Al. We observed an increase of 70% in *K* for Al–rGO composites with an rGO weight percentage of 1%. Several theoretical models were analyzed to understand the increment in *K* after the incorporation of rGO. Among all models, the Maxwell and Rayleigh models perfectly predict the experimental *K* values of the Al–rGO composites.

Experimental procedures

Fabrication of Al–rGO composites

Al blocks of different dimensions (Al 1050, 99.5%) were obtained from National Aluminum Company (NALCO, India), and rGO was purchased from Bottom Up Technologies Corporation (India). The dimension, layer number and thickness of the rGO sheets were <5 μ, 2–4 and 2–5 nm, respectively. The thermal conductivity of the graphene was 3000 $Wm^{-1}K^{-1}$. Al and rGO powder were used as received without any further purification. In a typical fabrication of the Al–rGO composite, the Al blocks were placed on an alumina boat and covered with rGO powder with the desired weight percentage. The boat was then kept in a quartz tube (2 in diameter) and heated at 730°C (± 5°C) in a single-zone tube furnace. The reactions were performed in an argon (Ar) atmosphere with a flow rate of 60 sccm to protect the samples from oxidation. The heating rate and time for all the reactions were maintained at 7°C/min and 2 h, respectively. The samples were cooled to room temperature in an Ar atmosphere and cleaned with isopropyl alcohol. The wettability of Al on the alumina surface of the boat was observed to be poor (contact angle > 90°). Bao *et al.* reported that the contact angle is 90° at 700°C and increases with increasing temperature [27]. Therefore, the Al blocks almost retained their pristine shape with slight deformation. A higher temperature (>800°C) may lead to better wettability; however, this was avoided owing to the formation of Al_4C_3 (Fig. S1 in the Supplementary Material). The densities of the Al–rGO composites measured via the Archimedes method were 2.11–2.62 g/cm^3; these results are summarized in Table S1 in the Supplementary Material.

Computational methodology

The first-principles calculations performed herein were based on the density functional theory (DFT) framework. For the calculations of the electron–phonon coupling constants, density functional perturbation theory [28] was employed, as implemented in the ABINIT code [29]. The exchange-correlation interaction was modelled through local density approximation. Only the valence electrons were considered explicitly using the plane-wave basis set with a kinetic energy cut-off of 60 Hartree. For the calculations of the electronic thermal conductivity (k_e), electrical conductivity (σ) and electron–phonon coupling constant (λ) of bulk Al with different lattice constants, a q-point grid of 4 × 4 × 4 and a k-point grid of 36 × 36 × 36 were used. The side and top view of the Al–rGO supercell are shown in Fig. 1.

Characterization techniques

X-ray diffraction (XRD) was conducted using a Bruker D8 Advance X-ray diffractometer with Cu Kα radiation (λ = 1.5406 Å) to understand the crystal structure of the composites. The presence of rGO in the Al matrix was confirmed via Raman spectroscopy (Renishaw inVia confocal Raman spectrometer). Scanning electron microscopy (SEM) images were captured in a dual-beam Zeiss Neon 40 microscope. An Oxford INCA x-act EDS attached to the SEM was employed to confirm the presence of rGO on the Al surface. Transmission electron microscopy (TEM) imaging was performed using a Jeol JEM 2010 with an electron beam of 200 keV. Four-probe electrical transport measurements were performed using a Keithley current source (Model: 6221) and a Keithley nanovoltmeter (Model: 2182A). A Linseis Xenon Flash Apparatus (XFA 600) was deployed to analyze the thermal properties. The microhardness (Vickers hardness) of the samples was tested using a Zwick/Roell Indentec instrument.

Results and discussion

Structural and morphological studies

Figure 2a shows the XRD pattern of pristine Al and Al–rGO composites with rGO weight percentages of 0.2, 0.6 and 1%. All

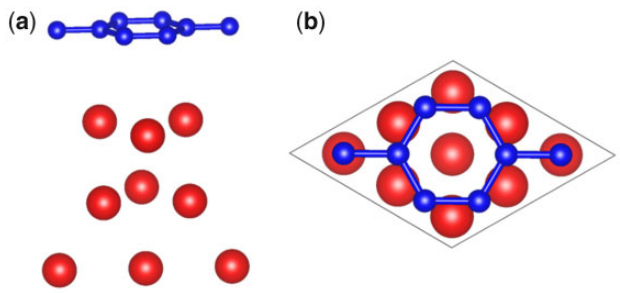

Figure 1. Schematic showing rGO 2 × 2 supercell adsorbed on the Al (111) surface. (**a**) Side view and (**b**) top view. The bigger and smaller spheres represent Al and C atoms, respectively.

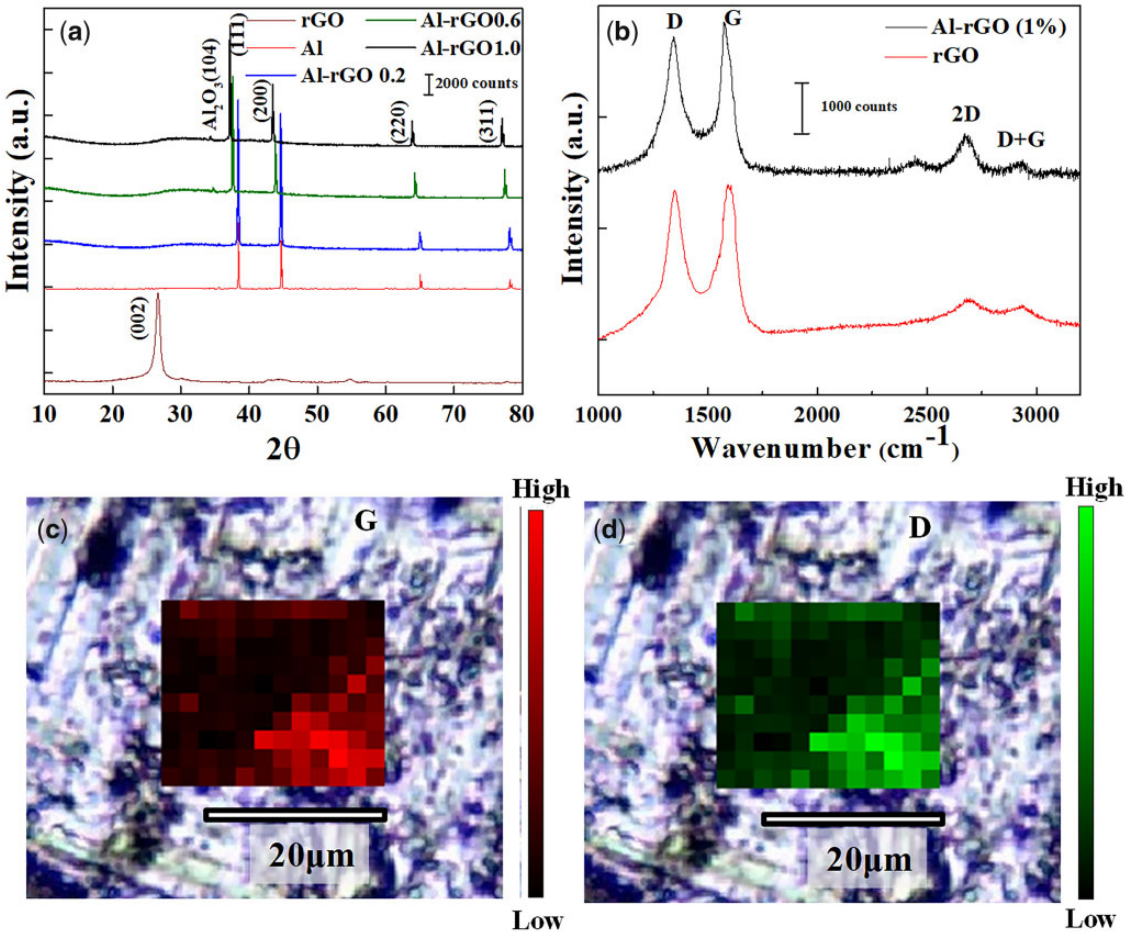

Figure 2. (**a**) XRD pattern of pristine Al and Al–rGO composites with different rGO weight percentages. (**b**) Raman spectra of pristine rGO and Al–rGO composites with an rGO weight percentage of 1%. Raman mapping was performed at (**c**) G and (**d**) D peaks of rGO.

Table 1. Calculated d-spacing and lattice parameters of Al–rGO composite samples with different rGO weight percentages

Sample detail	d-spacing	Lattice parameter (a)
Pristine Al	2.34 Å	4.05 Å
Al–rGO 0.2	2.34 Å	4.05 Å
Al–rGO 0.6	2.39 Å	4.12 Å
Al–rGO 1.0	2.41 Å	4.17 Å

pristine Al and Al–rGO composite samples show the cubic phase of Al with four peaks, corresponding to the (111), (200), (220) and (311) lattice planes. The absence of any extra peak in the Al–rGO composites indicates no formation of aluminum carbide (Al_4C_3) during the composite preparation. Further observations indicate a slight change in the 2θ values of the samples with different rGO weight percentages. This is attributed to the strain in Al owing to the inclusion of rGO. The changes in d spacing and the corresponding lattice parameters are shown in Table 1.

Raman studies of Al–rGO composites were conducted to realize the presence and distribution of rGO in the Al–rGO composites. Figure 2b shows the Raman spectra of pristine rGO and Al–rGO composites with an rGO weight percentage of 1%. The characteristic D, G and 2D bands of graphite are observed in the rGO and Al–rGO composite samples. The G band in rGO arises due to stretching of the C–C bond and the D band appears due to the defects, whereas the 2D band appears due to the second-order overtone of D [30]. In pristine rGO and the Al–rGO composites, the D band is observed at 1348 and 1344 cm^{-1} and the G band at 1583 and 1577 cm^{-1}, respectively. The D/G ratio of the pristine rGO and the Al–rGO composite has been calculated as 0.95 and 0.88. We believe the slight decrease in the D to G ratio in the Al–rGO composite is due to the further reduction of rGO during the composite preparation in the Ar atmosphere. The 2D and D + G peaks of rGO are observed at 2683 and 2937 cm^{-1}, which are red-shifted to 2675 and 2935 cm^{-1} in the Al–rGO composite. The shifts in the peaks are due to the change in the number of layers of rGO during the reaction [31]. Further, the presence of rGO in the Al matrix has been confirmed via Raman mapping. Figure 2c and d shows the Raman mapping of intensities using the Al–rGO composite sample with an rGO weight percentage of 1% (overlapped with optical imaging) at G and D peaks in the Raman spectra, respectively. Areas with a high concentration of rGO are shown in bright red or green, whereas those with a low concentration are shown as darker regions.

TEM was performed for the microstructural analysis of the Al–rGO composites. A TEM image of pristine rGO sheets shows the characteristic wrinkles and folds of rGO (Fig. 3a). Figure 3b shows rGO embedded in the Al matrix, and Fig. 3c shows a high-resolution TEM image indicating both Al (red box) and rGO (yellow box). The d-spacing of Al is calculated as 0.24 nm, which corresponds to the Al (111) plane. In the yellow box, rGO layers are clearly visible. These results further confirm the presence of rGO in Al. The microstructure of the Al–rGO composite has been further analyzed using SEM. SEM images of pristine Al and Al–rGO

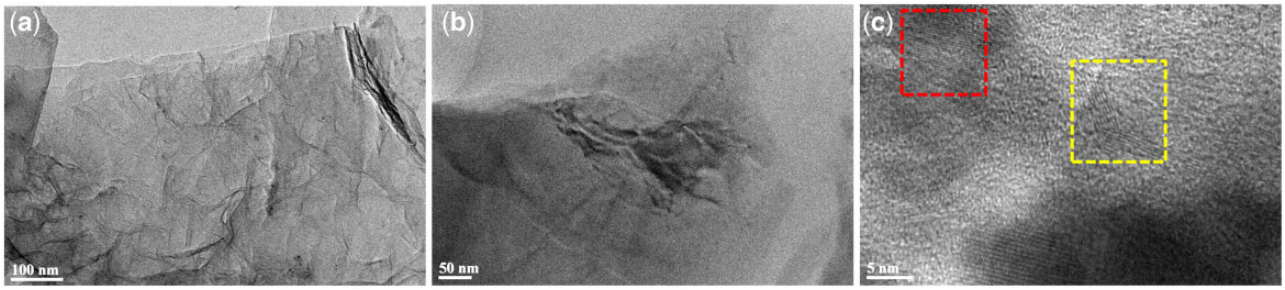

Figure 3. TEM image of (**a**) pristine rGO before preparing the composite, (**b**) rGO sheet embedded in Al matrix and (**c**) high-resolution TEM image showing both Al (left box) and rGO (right box).

samples are shown in Fig. S2a and b (Supplementary Materials), respectively. The pristine Al appears smooth and with uniform color compared with the Al–rGO composites. Understanding rGO in the Al matrix is difficult using SEM and is generally identified by contrast and surface shading [4, 32]. Elemental concentrations obtained from EDS at different accelerating voltages are shown in Supplementary Table S2. The detailed EDS analysis can be found in the Supplementary Materials (Section 3).

Study of interaction between Al and rGO

A non-spin polarized calculation under the DFT framework, as implemented in the Vienna Ab Initio Simulation Package code was performed to get more insight into the interaction between aluminum and graphene. The detailed methodology has been provided in the Supplementary Information (Section 4). The binding energy (ΔE) of graphene with the Al (111) surface was calculated using the following equation:

$$\Delta E = E_{Al-G} - (E_{Al} + E_G), \tag{1}$$

where E_{Al-G}, E_{Al} and E_G are the energies of the Al–G heterostructure, Al (111) surfaces and graphene monolayer, respectively. The equilibrium separation between the graphene monolayer and the Al surface was calculated to be 3.28 Å, whereas the binding energy per carbon atom was calculated to be 0.06 eV, indicating the weak adsorption of graphene in Al [33, 34].

Electronic structure of Al–rGO composites

The electronic band structure of the Al–rGO heterostructure has been calculated to observe the modification of the electronic properties of graphene on the Al surface. In pristine graphene, the valence band and conduction band converge at the K point, leading to a linear dispersion and forming a Dirac cone near the Fermi level (Fig. 4a). The projected band structure of the 2×2 supercell of graphene is shown in the figure, which indicates that open p_z orbitals of carbon atoms are responsible for the conical band structure. Conversely, the electronic band structure of graphene adsorbed on the Al (111) surface (Fig. 4b) indicates that the Dirac cone nature of graphene's band structure is preserved. In this case, the absence of *d*-states in the Al shows an extremely low tendency toward the open p_z of carbon in graphene. Consequently, a weak interaction with a large distance between Al and graphene is observed, which is called physisorption. Thus, the graphene layer is called physisorbed graphene.

Moreover, the conical point of graphene is shifted downward with respect to the Fermi level indicating some charge (electron) transfer between graphene and Al owing to differences in the work functions. For a better understanding of the charge-transfer scenario at the Al–G interface, the planar average charge density difference was calculated using the following equation:

$$\Delta n(z) = n_{Al-G}(z) - n_{Al}(z) - n_G(z), \tag{2}$$

where $n_{Al-G}(z)$, $n_{Al}(z)$ and $n_G(z)$ represent the plane-averaged charge densities of Al–rGO heterostructure, Al surfaces and graphene, respectively. From Fig. S3a (in the Supplementary Material), it is clear that the peak obtained at the interface is extremely small and Δn is localized at the interface, resembling a simple dipolar charge distribution. To visualize electron redistributions at the interface in a three-dimensional (3D) frame, charge-density differences for the above-described heterostructure have been plotted (Fig. S3b, in the Supplementary Material), which shows that the interspacing charge accumulation is extremely low and weakens the interaction between Al and graphene. In this case, the depletion regions located close to the metal indicate that the electronegativity of graphene exceeds that of the metal surface, which makes the graphene n-doped [35].

Electrical characterizations of Al–rGO composites

Figure 5a shows the voltage vs. current (VI) plots of pristine Al and Al–rGO composites with different rGO weight percentages. Resistances of the samples are calculated from the straight-line fitting of the V–I plots. The cross-sectional area and probe distance were kept the same for all the samples. Figure 5b shows the calculated resistivity of Al–rGO composites with different rGO weight percentages. The error bars in the graph indicate the standard deviation (~1–2%) calculated from five different measurements performed on a sample. At a lower percentage of rGO in Al, a marginally (~2.5%) decreased resistivity compared with pure Al has been observed. Pristine Al shows a resistivity of 3.8×10^{-8} Ω-m, whereas composites with an rGO weight percent of 0.2% show a resistivity of 3.7×10^{-8} Ω-m. Al–rGO composites with rGO weight percentages of 0.6% and 1% show higher resistivities, of 4.2×10^{-8} and 4.8×10^{-8} Ω-m, respectively. As listed in Table 1, the lattice constant of Al inside the Al–rGO matrix increases with an increase in the weight percentage of rGO. In other words, Al undergoes tensile strain in the Al–rGO composite. Up to a certain elastic strain (yield point), the strain sensitivity of resistance of metals or alloys goes to a minimum value, and beyond the yield point, the coefficient of strain sensitivity becomes positive [36]. This is attributed to the changes in the mean free path of the free electrons inside the metal.

Effect of electron–phonon coupling on electrical conductivity of Al–rGO composites

Electron–phonon coupling is crucial in deciding the electrical conductivity of metal–rGO systems. The variation of electrical

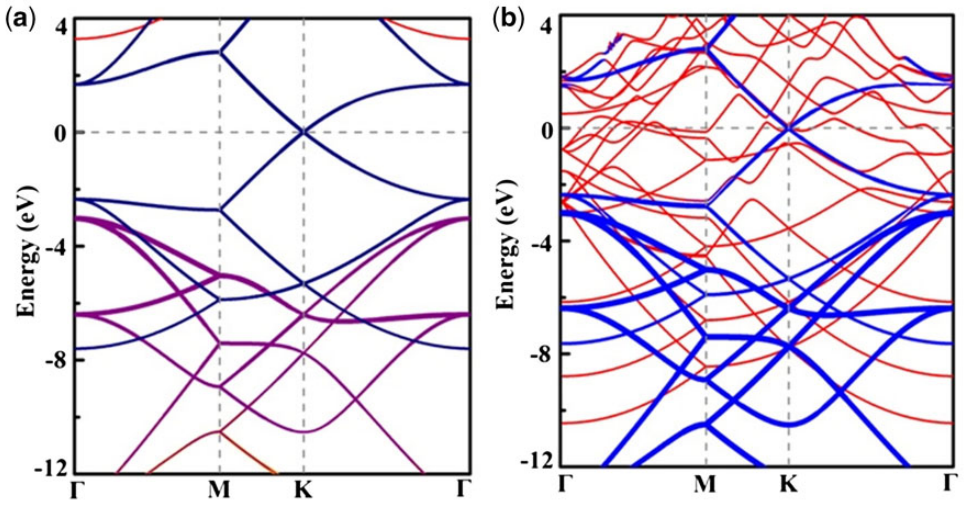

Figure 4. Projected electronic band structure of (**a**) 2 × 2 supercell of a graphene monolayer (s, $p_x + p_y$ and p_z orbital contributions are represented) and (**b**) Al–graphene heterostructure (Carbons orbital contributions are represented by thicker lines). The Fermi level is set at 0 eV.

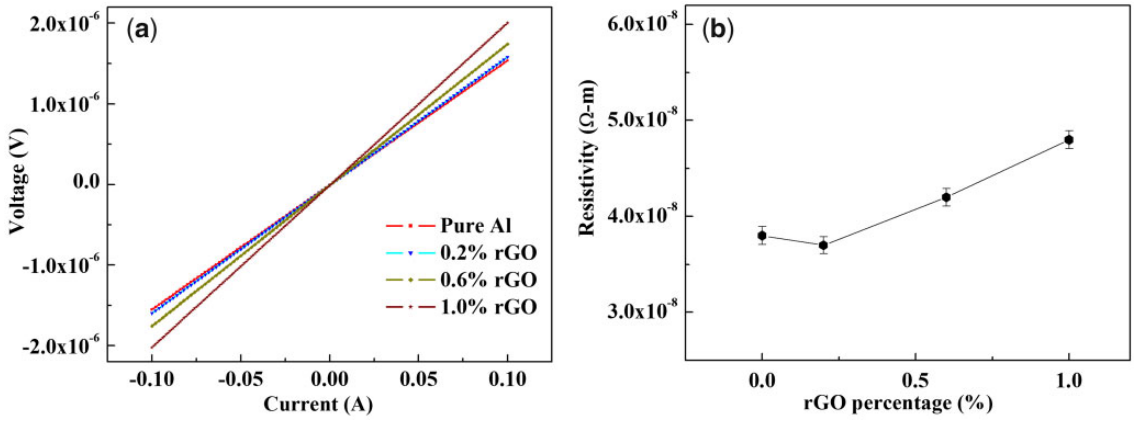

Figure 5. (**a**) Voltage vs. current plots of pristine Al and Al–rGO samples with different rGO weight percentages. (**b**) Changes in the resistivity with different weight percentages of rGO in the Al matrix.

Table 2. Electrical conductivity and electron–phonon coupling constants for pure Al and Al with different strains.

Material	Lattice constant (Å)	Electrical conductivity (σ) S/m ($\times 10^7$)	El-ph coupling constant (λ)
Pure Al	4.046	3.3914	0.54
Al (0.6% rGO)	4.139 (2.2% strain applied)	2.558	0.74
Al (1% rGO)	4.174 (3% strain applied)	2.268	0.83

conductivity with the weight percentage of rGO in the composites can be explained through the strength of the electron–phonon coupling constant (λ), which is obtained by averaging the electron–phonon couplings over the Fermi surface. From the XRD data, the interlayer distance (d) between the (111) planes of pure Al is calculated to be 2.34 Å. The d-spacing remains the same for an rGO weight percentage of 0.2 as pristine Al and increases with a further increase in rGO weight percentage in the Al–rGO composite (Table 1). Therefore, the incorporation of rGO in the Al matrix introduces a strain effect on the Al, resulting in a change in its lattice constant. A first-principles study has been performed to calculate the electrical conductivity and electron–phonon coupling constants of Al at different positive strains to understand the experimental results. The values of electrical conductivity and electron–phonon coupling constants for pure Al and Al with different strains are listed in Table 2. With an increase in the applied positive tensile strain, the electrical conductivity of Al decreases whereas the electron–phonon coupling constant increases. The energetic disorder created due to lattice thermal vibrations can be modified by applying strain to the system by changing the noncovalent forces between atoms or molecules [37]. With the higher percentage of rGO inside the metal matrix, the rate of collisions of electrons and phonons of Al with the phonons of filler rGO particles increases. Consequently, the effective mean free path is shortened, thereby decreasing the electrical conductivity.

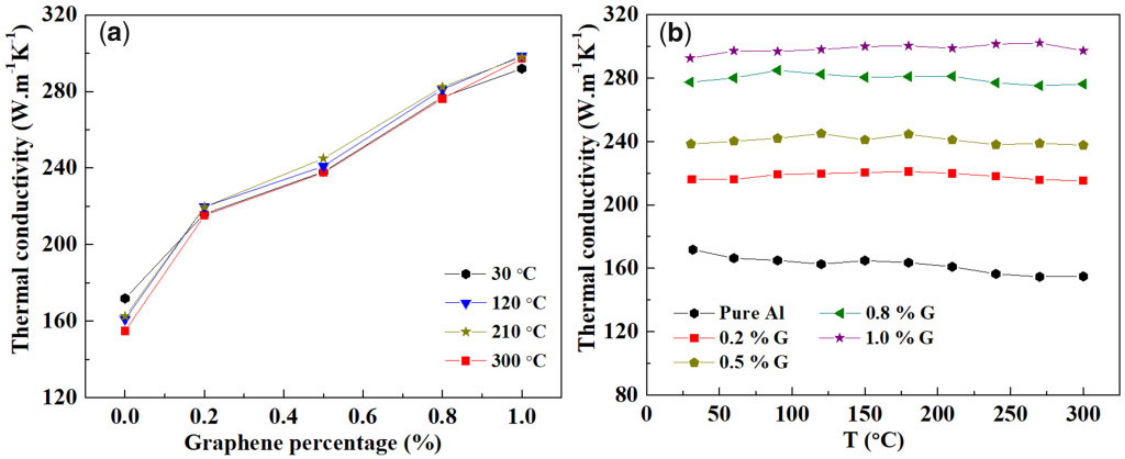

Figure 6. Thermal conductivity (**a**) as a function of rGO weight percentages at different temperatures and (**b**) as a function of temperature at different rGO weight percentages.

Thermal conductivity of Al–rGO composites

Thermal conductivity (*K*) of Al–rGO composites was measured as functions of rGO weight percentage and temperature as shown in Fig. 6a and b, respectively. The *K* values were calculated by measuring the thermal diffusivity and heat capacity. The *K* value increases sharply with an increasing rGO weight percentage (Fig. 6a) in Al–rGO composites and an enhancement of 70% has been observed at an rGO weight percentage of 1%. Pristine Al shows thermal conductivity of 175 $Wm^{-1}K^{-1}$ (standard deviation < 5% for all the thermal conductivity measurements), which is increased to 293 $Wm^{-1}K^{-1}$ for Al–rGO composites with rGO weight percentages of 1%. The value of *K* increases monotonically with increasing rGO content in the composite; however, we did not measure the *K* beyond 1% of rGO as the electrical conductivity significantly decreased for >1% of rGO in the composite. Additionally, *K* was measured at a temperature range of 30–300 K (Fig. 6b). For pristine Al, *K* decreases ∼10% at 300°C compared with room temperature; however, Al–rGO composites exhibit almost no change (< 2%) in *K* value with respect to temperature changes. The sharp increase in the *K* of the Al–rGO with increasing rGO content can be attributed to the extremely high thermal conductivity of rGO. The interfacial structure and the interaction between Al and rGO phases lead to better heat transfer at the interface. The primary heat carriers in Al and rGO are electrons and phonons, respectively. At the interface between Al and rGO, an energy channel exists to transfer heat from electrons to phonons. The interfacial thermal conductance of a metal–semimetal composite can be predicted primarily by two mechanisms [38, 39]: (i) the electrons and phonons of the metal couple with one another, and the energy can be transferred from these phonons to the phonons of the semimetal at the interface and (ii) electrons of the metals couple directly with the phonons of the semimetal. Thus, the electron–phonon coupling is crucial for heat transport inside the metal–rGO composite.

Physical properties such as thermal conductivity and electrical conductivity of the composites depend upon the volume fraction, geometrical structure, distribution and arrangement of filler particles (rGO) inside the metal matrix. Furthermore, the interaction between filler rGO and Al matrix is crucial in tuning these properties of the composites [40–42]. Several classical models, such as Maxwell, Son–Frey, Russell and Rayleigh, have been studied to understand the sharp increase in *K* with rGO weight percentage in the Al matrix. The volume fractions of the rGO and Al are considered the key parameters for all these theoretical models, and these models show excellent agreement with experiments for a wide range of filler particle volumes. At a high concentration, phonon scattering is highly affected by the interactions with rGO inside the mixture, resulting in a completely changed *K*. The equations for the conversion of weight fraction into volume fraction for the Al–rGO composite have been provided in the Supplementary Material.

First, two simple models are used to calculate the effective thermal conductivity of the Al–rGO composites. Consider the two phases (Al and rGO) as two plates that are oriented either perpendicular (series) or parallel (parallel) to the direction of heat flow, which is accordingly termed the series model or parallel model. The values obtained using these two models generally represent the lower and upper limits of effective thermal conductivity of the two-phase composite. In the series and parallel models, thermal conductivity is expressed as

$$K_{series} = \frac{1}{\frac{V_1}{k_1} + \frac{V_2}{k_2}}, \tag{3}$$

and

$$K_{para} = V_1 k_1 + V_2 k_2, \tag{4}$$

where V_1 and k_1 represent the volume fraction and thermal conductivity, respectively, of Al and V_2 and k_2 represent the corresponding parameters for rGO. Series and parallel models render thermal conductivity of 200 $Wm^{-1}K^{-1}$ and 900 $Wm^{-1}K^{-1}$ for Al–rGO composite with an rGO weight percentage of 1%. However, the experimentally obtained *K* values of Al–rGO composites are significantly different from the *K* values obtained using these two models. Furthermore, the Russell model and Son–Frey model are considered to calculate the effective thermal conductivity of Al–rGO composites and the results lie in between the values obtained in the series and parallel models. In both these models, rGO sheets (filler particles) are assumed to be distributed discontinuously and in a cubic-array manner in the continuous phase of the Al matrix [43, 44]. The Russell model is based on the concept of linear isotherms, whereas the Son–Frey model is based on the linear heat flow concept [45, 46]. The thermal conductivity of the composite can be calculated using the following equations

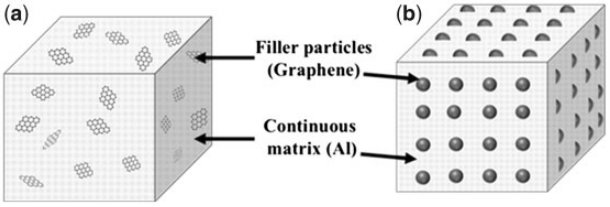

Figure 7. Schematic of various models of two-phase composites (**a**) Maxwell model and (**b**) Rayleigh model.

$$K_{Russell} = k_c \frac{1 - V_d^{\frac{2}{3}} + \frac{k_d}{k_c}.V_d^{\frac{2}{3}}}{1 - V_d^{\frac{2}{3}} + V_d + \frac{k_d}{k_c}(V_d^{\frac{2}{3}} - V_d)}, \quad (5)$$

$$K_{Son-Frey} = k_c \frac{1 - V_d^{\frac{1}{3}} + V_d + \frac{k_c}{k_d}.(V_d^{\frac{1}{3}} - V_d)}{1 - V_d^{\frac{1}{3}} + \frac{k_c}{k_d}.V_d^{\frac{1}{3}}}, \quad (6)$$

where V_d and V_c are the volume fraction of dispersed rGO fillers and continuous Al matrix in the composite, respectively, and k_d and k_c are the thermal conductivities of the respective phases. As these models describe minor phase dispersion within a matrix of the major phase, the values for effective conductivity are close to the experimental results.

The Maxwell model [47] and the Rayleigh model [48] can correlate the theoretical and experimental values of the effective thermal conductivity of Al–rGO composite up to a certain amount of filler content. In Maxwell's model, rGO is considered as spherical filler particles of thermal conductivity k_d, which are dispersed discontinuously in the continuous Al matrix of thermal conductivity k_c, as shown in Fig. 7a. Here, interactions between filler particles are assumed to be negligible and the model is valid for lower volume fractions (up to 25%) of filler [49, 50]. Rayleigh modified Maxwell's model by considering the distribution of spherical filler particles inside the continuous matrix in a cubic manner (Fig. 7b). In his model, thermal interactions between filler particles are considered. Consequently, for higher filler content the Rayleigh model renders a better match to the experimental values than Maxwell's model. The effective thermal conductivity of the composite for the two models is provided by the following equations:

$$k_{Maxwell} = k_c \left(1 + \frac{3V_d}{\left(\frac{k_d + 2k_c}{k_d - k_c}\right) - V_d}\right) \quad (7)$$

$$k_{Rayleigh} = k_c \left(1 + \frac{3V_d}{\left(\frac{k_d + 2k_c}{k_d - k_c}\right) - V_d + 1.569\left(\frac{k_d - k_c}{3k_d - 4k_c}\right)V_d^{\frac{10}{3}} + \cdots}\right). \quad (8)$$

Results obtained from equations (7) and (8) are similar for volume fractions of filler particles up to 25%. In equation (8), higher-order components in the denominator are ignored. If the second term of the denominator is ignored, then the Rayleigh equation is reduced to the Maxwell equation.

Figure 8 shows several curves that represent the effective *K* of Al–rGO composites predicted from various models. As discussed earlier, the values obtained using the series–parallel models highly deviate from the experimental values whereas the values calculated using the Russell model and Son–Frey model are relatively closer to the experimental values. Both the Maxwell and Rayleigh models predict almost the same results as those obtained experimentally. Because the weight percentages of rGO are only taken up to 1% in the composite, both Maxwell and Rayleigh models provide similar results. The filler particles develop continuous conductive networks for high rGO contents, whereas the filler particles are dispersed without developing a conductive network in the composite for low volume fractions.

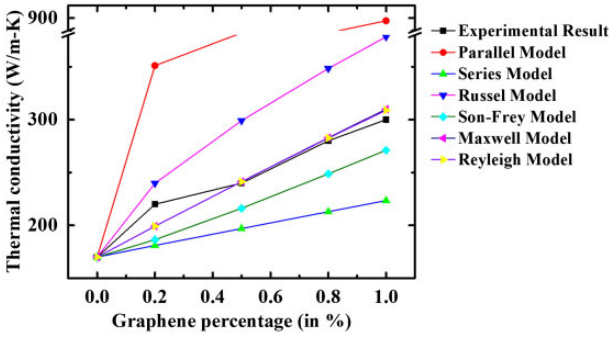

Figure 8. Effective thermal conductivity of Al–rGO composites at different weight percentages of rGO was estimated using various models.

The interfacial structure and the interaction between Al and rGO phases improve heat transfer at the interface [51]. With an increase in volume fraction (weight fraction) of rGO in the composite, the effective thermal conductivity increases rapidly. Because the as-synthesized samples contain dilute concentrations of filler particles (rGO), the heat flux lines created by one particle are not affected by other neighboring particles owing to the large spacing between filler particles. Furthermore, with an increase in rGO content inside the metal matrix, discontinuous phases slowly modify into a continuous network rather than agglomerating into clusters. This leads to the availability of more phase space through which heat carrier phonons travel with less scattering. This increases the uniform flow of heat in a particular direction and enhances the effective thermal conductivity of the composite. In modern technology, the dimensions of electronic devices are approaching the nanoscale; and heat dissipation of the integrated circuits has become a key concern. Therefore, the sharp increase in thermal conductivity of Al is an extremely encouraging observation from the application perspective.

Microhardness measurements

A microhardness test was performed using a Vickers indenter with a 2 kgf (19.6 N) force on the measurement points. Measurements were recorded from 10 indentations to determine the average microhardness value. Figure 9 shows the microhardness as a function of rGO percentage in Al–rGO composites. Error bars in the graph indicate the standard deviation in the average of 10 measurement values. The hardness of the Al–rGO composites is represented in the Vickers pyramid number (HV). Vickers hardness is calculated as follows [52]:

$$HV = 0.18 \times F/d^2, \quad (9)$$

where F is the applied force and d is the diagonal distance of the diamond indenter. Pristine Al has a Vickers hardness value of 36 (±1) HV and the hardness value marginally increased to 38 (±1) HV at rGO concentrations of 0.2% and 0.6% weight percentages. However, an increase in rGO weight percentages does not increase the microhardness value further. The hardness value was found to be 36 (±1) HV for an rGO weight percentage of 1%. Thus, the composite formation does not affect the hardness of Al.

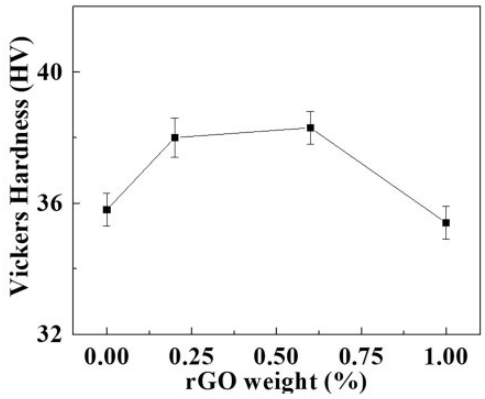

Figure 9. Change in the microhardness for different weight percentages of rGO in Al–rGO composites.

Conclusions

Al–rGO composites have been prepared by incorporating rGO in molten Al in an Ar atmosphere. Electrical, thermal and mechanical properties of Al–rGO composite samples with different rGO weight percentages have been analyzed. Electrical transport measurements of the Al–rGO samples show that for an rGO weight percentage of 0.2%, the electrical conductivity increases by ∼2.5%, and then decreases monotonically for higher rGO percentages. DFT calculations reveal that the electron–phonon coupling constant increases with further increase (>0.2%) in the rGO content in the Al matrix and electrical conductivity decreases. Thermal conductivity of the Al–rGO composite with an rGO weight percentage of 1% shows an increment of 70% compared with pristine Al. The interfacial structure and the interaction between Al and rGO are believed to facilitate better heat transfer at the interface. Various theoretical models have been analyzed to understand the increase in thermal conductivity after the incorporation of rGO. Among all the models, the Maxwell and Rayleigh models almost exactly match the experimentally obtained thermal conductivity values. Microhardness follows the same trend as electrical conductivity. Microhardness increases up to a small rGO weight percentage and then decreases with increasing rGO content. In conclusion, electrical, thermal and mechanical properties of Al–rGO composites vary differently with increasing rGO weight percentage in the Al matrix. A 70% increase in thermal conductivity without deteriorating electrical conductivity and microhardness of Al by the fabrication of Al–rGO composite is very encouraging and has not been reported earlier. The facile approach of this preparation method makes it easily scalable for industrial production.

Supplementary data

Supplementary data is available at *Oxford Open Materials Science Journal* online.

Data availability

The data underlying this article will be shared on reasonable request to the corresponding author.

Authors' contributions

Arijit Mitra (Data curation [lead], Formal analysis [equal], Investigation [lead], Methodology [lead], Writing—original draft [lead]), Mihir Ranjan Sahoo (Data curation [supporting], Formal analysis [supporting], Investigation [equal], Methodology [supporting], Writing—original draft [supporting]), Aiswarya Samal (Data curation [supporting], Formal analysis [supporting], Investigation [supporting], Writing—original draft [supporting]), Sunil Kumar Pradhan (Data curation [supporting], Formal analysis [supporting]), Balaram Polai (Data curation [supporting], Formal analysis [supporting]), Krishna Rani Sahoo (Data curation [supporting], Investigation [supporting]), Subrat Kar (Funding acquisition [equal]), Bijoy Kumar Satpathy (Conceptualization [equal], Project administration [equal], Supervision [supporting], Writing—review and editing [supporting]), Tharangattu N. Narayanan (Resources [supporting], Writing—review and editing [supporting]), Pulickel M. Ajayan (Conceptualization [supporting], Resources [supporting], Writing—review and editing [supporting]), Parlapalli V. Satyam (Conceptualization [supporting], Formal analysis [supporting], Resources [lead], Supervision [supporting], Writing—review and editing [equal]) and Prof. Saroj K. Nayak (Conceptualization [equal], Funding acquisition [equal], Project administration [lead], Resources [equal], Supervision [lead], Writing—review and editing [lead]).

Funding

National Aluminium Company (NALCO), Bhubaneswar has been gratefully acknowledged for the funding of the work (Grant number: RP-274). Part of this work has also been supported by the Ministry of Human Resource Development (MHRD), India, through a Centre of Excellence grant and the Department of Science and Technology (DST–MES), India.

Conflict of interest statement

The authors declare that they have no conflict of interest or personal relationships that could have appeared to influence the work reported in this paper.

Acknowledgements

We sincerely acknowledge CSIR–Advanced Materials and Processes Research Institute, Bhopal for their assistance in thermal conductivity measurements. The simulations and computations were supported in part by the SAMKHYA: High-Performance Computing Facility provided by the Institute of Physics (IOP), Bhubaneswar.

References

[1]. Kaczmar JW, Pietrzak K, Włosiński W. The production and application of metal matrix composite materials. *J Mater Process Technol* 2000;**106**:58–67.

[2]. Xu J, Zou B, Tao S *et al.* Fabrication and properties of Al_2O_3–TiB_2–TiC/Al metal matrix composite coatings by atmospheric plasma spraying of SHS powders. *J Alloys Compd* 2016;**672**:251–59.

[3]. Mavhungu ST, Akinlabi ET, Onitiri MA *et al.* Aluminum matrix composites for industrial use: advances and trends. *Procedia Manuf* 2017;**7**:178–82.

[4]. Liu J, Khan U, Coleman J *et al.* Graphene oxide and graphene nanosheet reinforced aluminium matrix composites: powder synthesis and prepared composite characteristics. *Mater Des* 2016;**94**:87–94.

[5]. Chawla N, Chawla KK. *Metal Matrix Composites*. New York: Springer, 2006.

[6]. Miranda AT, Bolzoni L, Barekar N *et al.* Processing, structure and thermal conductivity correlation in carbon fibre reinforced aluminium metal matrix composites. *Mater Des* 2018;**156**: 329–39.

[7]. Pradhan SK, Sahoo MR, Ratha S *et al.* Graphene-incorporated aluminum with enhanced thermal and mechanical properties for solar heat collectors. *AIP Adv* 2020;**10**:065016.

[8]. Wang X, Gong L-X, Tang L-C *et al.* Temperature dependence of creep and recovery behaviors of polymer composites filled with chemically reduced graphene oxide. *Compos Part A* 2015; **69**:288–98.

[9]. Castro Neto AH, Guinea F, Peres NMR *et al.* The electronic properties of graphene. *Rev Mod Phys* 2009;**81**:109–62.

[10]. Geim AK, Novoselov KS. The rise of graphene. *Nat Mater* 2007; **6**:183–191.

[11]. Li Z, Guo Q, Li Z *et al.* Enhanced mechanical properties of graphene (reduced graphene oxide)/aluminum composites with a bioinspired nanolaminated structure. *Nano Lett* 2015;**15**: 8077–83.

[12]. Wang J, Li Z, Fan G *et al.* Reinforcement with graphene nanosheets in aluminum matrix composites. *Scr Mater* 2012;**66**: 594–7.

[13]. Boostani AF, Yazdani S, Mousavian RT *et al.* Strengthening mechanisms of graphene sheets in aluminium matrix nanocomposites. *Mater Des* 2015;**88**:983–9.

[14]. Bartolucci SF, Paras J, Rafiee MA *et al.* Graphene–aluminum nanocomposites. *J Mater Sci Engg A* 2011;**528**:7933–7.

[15]. Shin S, Choi H, Shin J *et al.* Strengthening behavior of few-layered graphene/aluminum composites. *Carbon* 2015;**82**: 143–51.

[16]. Yolshina LA, Muradymov RV, Korsun IV *et al.* Novel aluminum-graphene and aluminum-graphite metallic composite materials: synthesis and properties. *J Alloys Compd* 2016; **663**:449–59.

[17]. Fadavi Boostani A, Tahamtan S, Jiang ZY *et al.* Enhanced tensile properties of aluminium matrix composites reinforced with graphene encapsulated SiC nanoparticles. *Compos Part A Appl Sci Manuf* 2015;**68**:155–63.

[18]. Nie J-h, Jia C-c, Shi N *et al.* Aluminum matrix composites reinforced by molybdenum-coated carbon nanotubes. *Int J Miner Metall* 2011;**18**:695–702.

[19]. Liu Z, Xiao B, Wang W *et al.* Tensile strength and electrical conductivity of carbon nanotube reinforced aluminum matrix composites fabricated by powder metallurgy combined with friction stir processing. *J Mater Sci Technol* 2014;**30**:649–55.

[20]. Zeng Y, Li T, Yao Y *et al.* Thermally conductive reduced graphene oxide thin films for extreme temperature sensors. *Adv Funt Mater* 2019;**29**:1901388.

[21]. Kwon H, Mondal J, AlOgab KA *et al.* Graphene oxide-reinforced aluminum alloy matrix composite materials fabricated by powder metallurgy. *J Alloys Compd* 2017;**698**:807.

[22]. Hu Z, Chen F, Xu J *et al.* 3D printing graphene aluminum nanocomposites. *J Alloys Compd* 2018;**746**:269.

[23]. Pourmand NS, Asgharzadeh H. Aluminum matrix composites reinforced with graphene: a review on production, microstructure, and properties. *Crit Rev Solid State Mater Sci* 2020;**45**: 289–337.

[24]. Zhou W, Fan Y, Feng X *et al.* Creation of individual few-layer graphene incorporated in an aluminum matrix. *Compos Part A Appl Sci Manufact* 2018;**112**:168.

[25]. Dasari BL, Morshed M, Nouri JM *et al.* Mechanical properties of graphene oxide reinforced aluminium matrix composites. *Compos Part B Eng* 2018;**145**:136.

[26]. Naplocha K, Granat K. Dry sliding wear of Al/Saffil/C hybrid metal matrix composites *Wear* 2008;**265**:1734–40.

[27]. Bao S, Tang K, Kvithyld A *et al.* Wettability of aluminum on alumina. *Metall Mater Trans B* 2011;**42**:1358–66.

[28]. Baroni S, De Gironcoli S, Dal Corso A *et al.* Phonons and related crystal properties from density-functional perturbation theory. *Rev Mod Phys* 2001;**73**:515.

[29]. Gonze X, Amadon B, Anglade P-M *et al.* ABINIT: first-principles approach to material and nanosystem properties. *Comput Phys Commun* 2009;**180**:2582–615.

[30]. Malard L, Pimenta M, Dresselhaus G *et al.* Raman spectroscopy in graphene. *Phys Rep* 2009;**473**:51–87.

[31]. Limbu TB, Mendoza F, Barrionuevo D *et al.* Study on the optical and electrical properties of tetracyanoethylene doped bilayer graphene stack for transparent conducting electrodes. *AIP Adv* 2016;**6**:035319.

[32]. Dasari BL, Morshed M, Nouri JM *et al.* Mechanical properties of graphene oxide reinforced aluminium matrix composites. *Compos B Eng* 2018;**145**:136–44.

[33]. Hafner J. Ab-initio simulations of materials using VASP: Density-functional theory and beyond. *J Comput Chem* 2008;**29**: 2044–78.

[34]. Kresse G, Furthmüller J. Efficient iterative schemes for ab initio total-energy calculations using a plane-wave basis set. *Phys Rev B* 1996;**54**:11169–86.

[35]. Wu P, Huang M, Yin N *et al.* The modulation effect of MoS_2 monolayers on the nucleation and growth of Pd clusters: first-principles study. *Nanomaterials* 1029;**9**:395.

[36]. Kuczynski GC. Effect of elastic strain on the electrical resistance of metals. *Phys Rev* 1954;**94**:61–4.

[37]. Ruggiero MT, Ciuchi S, Fratini S *et al.* Electronic structure, electron-phonon coupling, and charge transport in crystalline rubrene under mechanical strain. *J Phys Chem C* 2019;**123**: 15897–907.

[38]. Majumdar A, Reddy P. Role of electron–phonon coupling in thermal conductance of metal–nonmetal interfaces. *Appl Phys Lett* 2004;**84**:4768–70.

[39]. Sadasivam S, Waghmare UV, Fisher TS. Electron-phonon coupling and thermal conductance at a metal-semiconductor interface: first-principles analysis. *J Appl Phys* 2015;**117**: 134502.

[40]. Radzuan NAM, Sulong AB, Sahari J. A review of electrical conductivity models for conductive polymer composite. *Int J Hydrog Energy* 2017;**42**:9262–73.

[41]. Stankovich S, Dikin DA, Dommett GH *et al.* Graphene-based composite materials. *Nature* 2006;**442**:282–6.

[42]. Taherian R, Hadianfard MJ, Golikand AN. A new equation for predicting electrical conductivity of carbon-filled polymer composites used for bipolar plates of fuel cells. *J Appl Polym Sci* 2013;**128**:1497–509.

[43]. Poirier DR, Geiger G. *Transport phenomena in materials processing*. Warrendale, PA: TMS Publications, 1994.

[44]. Sterling EA, Stolk J, Hafford L *et al.* Sodium borohydride reduction of aqueous silver-iron-nickel solutions: a chemical route to synthesis of low thermal expansion–high conductivity Ag-invar alloys. *Metall Mater Trans A* 2009;**40**:1701–9.

[45]. Frey S. Uber die elektrische leitfabrigketeit binaer aggregate *Z Elecktrochem* 1932;**38**:260–74.

[46]. Russell HW. Principles of heat flow in porous insulators. *J Am Ceram Soc* 1935;**18**:1–5.
[47]. Maxwell JC. *A Treatise on Electricity and Magnetism*. Oxford: Clarenton Press Series, 1873.
[48]. Rayleigh L, Sec RS. LVI. On the influence of obstacles arranged in rectangular order upon the properties of a medium. *J Sci* 1892;**34**:481–502.
[49]. Bird RB, Stewart WE, Lightfoot EN *et al. Introductory Transport Phenomena*. New York: Wiley, 2015.
[50]. Pietrak K, Wiśniewski TS. A review of models for effective thermal conductivity of composite materials. *J Power Technol* 2014; **95**:14–24.
[51]. Zheng L, Zheng H, Huo D *et al.* N-doped graphene-based copper nanocomposite with ultralow electrical resistivity and high thermal conductivity. *Sci Rep* 2018;**8**:9248.
[52]. Franco AR Jr, Pintaúde G, Sinatora A *et al.* The use of a Vickers indenter in depth sensing indentation for measuring elastic modulus and Vickers hardness. *Mat Res* 2004;**7**:483–91.